https://doi.org/10.18321/ectj1542

Optimization of the Porous Structure of Carbon Electrodes for Hybrid Supercapacitors with a Redox Electrolyte Based on Potassium Bromide

V.V. Pavlenko[1,2], K.M. Temirkulova[1,2], A.Yu. Zakharov[2], Y.A. Aubakirov[1], Zh.E. Ayaganov[1,2]*

[1]al-Farabi Kazakh National University, 71 al-Farabi ave., Almaty, Kazakhstan
[2]Institute of Combustion Problems, 172 Bogenbay batyr str.., Almaty, Kazakhstan

Article info

Received:
7 August 2023

Received in revised form:
16 September 2023

Accepted:
24 October 2023

Keywords:
Hybrid capacitor
Porous structure
Mass balancing
Redox electrolyte
Potassium bromide

Abstract

This work investigates the electrochemical behavior of hybrid supercapacitors with carbon-based electrodes of different porosity using 5M $NaNO_3$ + 0.5M KBr electrolyte to optimize energy storage processes. Three types of carbon materials were synthesized: activated carbon from rice husk (RH) with a specific surface area of ~2300 m^2/g and pore size < 1 nm, and templated carbons from magnesium citrate (MP-8) and glucose with SiO_2 as a template (G7), having surface areas of 1976 and 1320 m^2/g and pore sizes of 3.4 and 7 nm, respectively. The microporous structure of activated carbon (AC) obtained from RH shows limitations in the diffusion of electrolyte ions, which affects the charge-discharge kinetics. In contrast, the larger mesoporous structures of templated carbons promoted better adsorption and ion transport, significantly affecting the dynamics of redox reactions. The RH/MP-8 hybrid capacitor, combining high surface area and large pore size, demonstrated a 54% increase in specific capacitance, 128% increase in specific energy and 51% increase in energy efficiency at high current densities of 5 A/g, comparing to the symmetric RH/RH hybrid capacitor. This study highlights the critical importance of the relationship between electrode pore structure and electrolyte composition for optimizing supercapacitor performance, which provides valuable information for the development of efficient energy storage technologies.

1. Introduction

In recent years, there has been an increasing demand for renewable energy and electric vehicles worldwide. However, for a successful global green energy transition, the development of energy storage systems such as capacitors, batteries, and supercapacitors is needed, alongside the generation systems [1, 2]. Among energy storage systems, electric double layer capacitors (EDLCs) and hybrid supercapacitors have attracted considerable attention. High specific capacitance and power density allow hybrid capacitors to be used in applications requiring fast energy transfer, such as regenerative braking in hybrid and electric cars, or in smoothing fluctuations in electricity generated by wind farms [3–6].

Hybrid supercapacitors combine the advantages of classical EDLCs, which store energy in the electrical double layer through electrostatic charge separation, and reversible redox reactions. This combination provides hybrid supercapacitors with increased capacitance and energy density compared with classical EDLCs, as well as higher power density compared with batteries [7–9].

There are two main methods for improving the performance of hybrid supercapacitors: developing new electrode materials and optimizing electrolytes [10, 11]. There are two main types of electrolytes in hybrid supercapacitors: aqueous and organic.

*Corresponding author.
E-mail address: zhanibek13@gmail.com

Aqueous electrolytes have several distinct advantages over organic electrolytes, including higher conductivity, environmental sustainability, and cost effectiveness [10]. In this work, we used the aqueous electrolyte 5M $NaNO_3$ + 0.5M KBr because of its high electrical conductivity and the ability of $NaNO_3$ to inhibit metal corrosion by bromine ions [11].

Typical materials used as electrodes in EDLCs include activated carbons, carbon aerogels, and other carbon nanomaterials [12–14]. Among them, activated and templated carbons are the most widely used due to its high specific surface area, low cost, simple and scalable fabrication process, and a wide range of available precursors [15, 16].

However, despite the extensive research on the development of new carbon materials, there are comparatively few studies that focus on optimizing the porous structure of electrodes for specific electrolytes. The present work focuses on the optimization of a hybrid capacitor using the promising aqueous electrolyte 5M $NaNO_3$ + 0.5M KBr by fine-tuning the porous structure of carbon electrodes.

2. Experimental

2.1. Synthesis of porous carbon materials

Porous carbon materials with different structures were synthesized using chemical activation and template synthesis methods. Activated carbon from rice husk was obtained by carbonizing the feedstock sourced from farms in the Almaty region of Kazakhstan at 550 °C in a nitrogen atmosphere for 60 min. The obtained carbonizate was leached with a 2.5M NaOH solution at 90 °C, followed by washing with distilled water until a neutral pH was reached. To develop a highly porous structure, the carbonized rice husk was mixed with dry KOH in a 1:4 mass ratio. This mixture was placed in a stainless-steel reactor, which was heated to 350 °C at a rate of 10 °C/min, holding isothermally for 30 minutes. Then the temperature was risen to 800 °C at the same rate and kept for 60 min in a nitrogen atmosphere. The resulting activated carbon was washed with distilled water until a neutral pH was reached and then dried in a vacuum at 90 °C [17, 18].

Template carbon from magnesium citrate (Laborfarma LLP) was obtained by carbonizing the initial salt in a nitrogen atmosphere for 120 min at 900 °C. The carbonizate was treated with a 3M HCl solution at room temperature for 24 h. The resulting templated carbon was washed with distilled water to neutral pH and then dried in a vacuum at 90 °C [19].

The 30% aqueous colloidal suspension of SiO_2 with an average particle size of 7 nm (Ludox SM30 colloidal silica, Sigma-Aldrich) was used as template to obtain nanoporous carbon from glucose (Laborfarma LLP). The starting components were stirred in a 1:1 mass ratio (based on the dry weight of the template) on a magnetic stirrer for one hour. Caramelization was performed at 160 °C for 8 h to fix the template in the matrix. Carbonization was performed in a quartz tube reactor at 800 °C in a nitrogen atmosphere for 2 h. To remove the SiO_2 template, the carbonizate was leached with a 3M NaOH solution at 90 °C for 24 h. The resulting templated carbon was washed with distilled water until a neutral pH was reached and then dried in a vacuum at 90 °C [17].

To remove the surface functional groups, all obtained carbons were thermally treated at 800 °C in a quartz tube reactor under nitrogen flow at a rate of 150 mL/min for 2 h. The post-treated activated carbon from rice husk, templated carbon from magnesium citrate, and templated carbon from glucose are referred to as RH, MP-8, and G7, respectively.

2.2. Materials characterization

The adsorption and desorption isotherms of gaseous nitrogen on the carbon samples were measured using a Micromeritics ASAP 2020 surface area and pore size analyzer at -196 °C. Before measurements, the carbon samples were vacuum dried at 350 °C for 12 h to remove any adsorbed gases and moisture. The specific surface area of each sample was determined using the Brunauer–Emmett–Teller (BET) method. For pore size distribution analysis, two-dimensional nonlocal density functional theory (2D-NLDFT) was employed. The average pore size of the samples was calculated using the Dubinin–Radushkevich equation.

The Raman scattering spectra were obtained using a Solver Spectrum, NT-MDT instrument with a blue solid-state laser at a wavelength of 473 nm and a spectral resolution of 4 cm^{-1}. The graphitization value G(%) of the obtained samples was determined by the formula [20]:

$$G, \% = \frac{A(G)}{\sum_{500}^{2000} A} \times 100\% \quad (1)$$

where A(G) is the area of the G band region, and $\sum_{500}^{2000} A$ is the sum of the areas of all peaks as a result of decomposition under the regions of the D and G bands.

The surface morphology of the samples was investigated using a Quanta 200i 3D scanning electron microscope (SEM) at an accelerating voltage of HV=15kV.

2.2. Free-standing electrode's fabrication

Freestanding electrodes were prepared by mixing 85 wt.% of the obtained carbons with 5 wt.% conductive additive (TIMCAL SUPER C45 Conductive Carbon Black) and 10 wt.% binder (60% aq. dispersion of PTFE, Sigma-Aldrich). The mixture was stirred on a magnetic stirrer overnight at a heating temperature of 70 °C, with a small amount of isopropanol added to achieve a liquid consistency. Slow evaporation allowed all the ingredients to mix evenly and continued until a clay-like mass was formed. The resulting electrode material was rolled at least 20 times on a flat hard surface using metal rollers with a 150 µm notch, to better mix the components and compact the electrodes. The formed freestanding electrodes were dried in a vacuum oven at 90 °C overnight, after which electrodes of the required size were cut out using punches of different diameters. The mass balance was maintained by varying the area of the positive electrode, while the size of the negative electrode remained unchanged.

2.3. Electrochemical and structure characterization

In this study, various combinations of hybrid cells were investigated to evaluate their electrochemical behavior. Table 1 provides an overview of the different hybrid cell configurations, specifying the number of full cells and those with a reference electrode.

Table 1. Configurations of various cell types

#	Cells with reference electrode (vs Ag/AgCl)	Hybrid cell configuration	
		Negative electrode (-)	Positive electrode (+)
1	Activated carbon from rice husk (RH)	RH	RH
2	Templated carbon from magnesium citrate (MP-8)	RH	MP-8
3	Templated carbon from glucose (G7)	RH	G7

Electrochemical studies, such as cyclic voltammetry (CV) and galvanostatic charge-discharge (GCD), were conducted using the Elins P-40X potentiostat/galvanostat (Russia). To determine the working voltage of the cell and for further mass balancing, measurements were carried out in three-electrode Swagelok-type cells with stainless steel current collectors and an Ag/AgCl reference electrode. The explored potential range of the negative electrode varied from -1.3 to 0 V, and from 0 to 1 V for the positive electrode. Aqueous solution of 5M $NaNO_3$ + 0.5M KBr was used as the redox electrolyte, and Whatman GF/A glass fiber filter was used as the separator.

After determining the working potential window for the positive and negative electrodes, mass balancing was carried out based on the following equation [21]:

$$C_+ \times V_+ \times m_+ = C_- \times V_- \times m_- \quad (2)$$

where C is the specific capacitance of the electrode (F/g) at a given potential, V is the maximum working potential of the electrode (V), and m is the mass of the electrode (g).

To calculate the specific capacitance of electrodes in a three-electrode system, the following formula was used:

$$C_{el} = \frac{1}{2 \times m_w v (V_b - V_a)} \int_{V_a}^{V_b} IdV \quad (3)$$

where C_{el} is the specific capacitance (F/g), V_b–V_a is the final and initial potential (V), I is the current (A), v is the scan rate (V/s), and m_w is the mass of the working electrode (g).

For calculating the specific capacitance of electrodes in a two-electrode system, the following formula was used:

$$C_{el} = \frac{2}{m_{total} \times v (V_b - V_a)} \int_{V_a}^{V_b} IdV \quad (4)$$

where C_{el} is the specific capacitance (F/g), V_b–V_a is the final and initial potential (V), I is the current (A), v is the scan rate (V/s), and m_{total} is the mass of the working electrode (g).

The methodology for calculating based on GCD data was similar to that presented in the work [2].

3. Results and discussion

3.1. Structure characterization

Scanning electron microscopy was employed as an effective method for investigating the morphology of the obtained porous carbon materials. As can

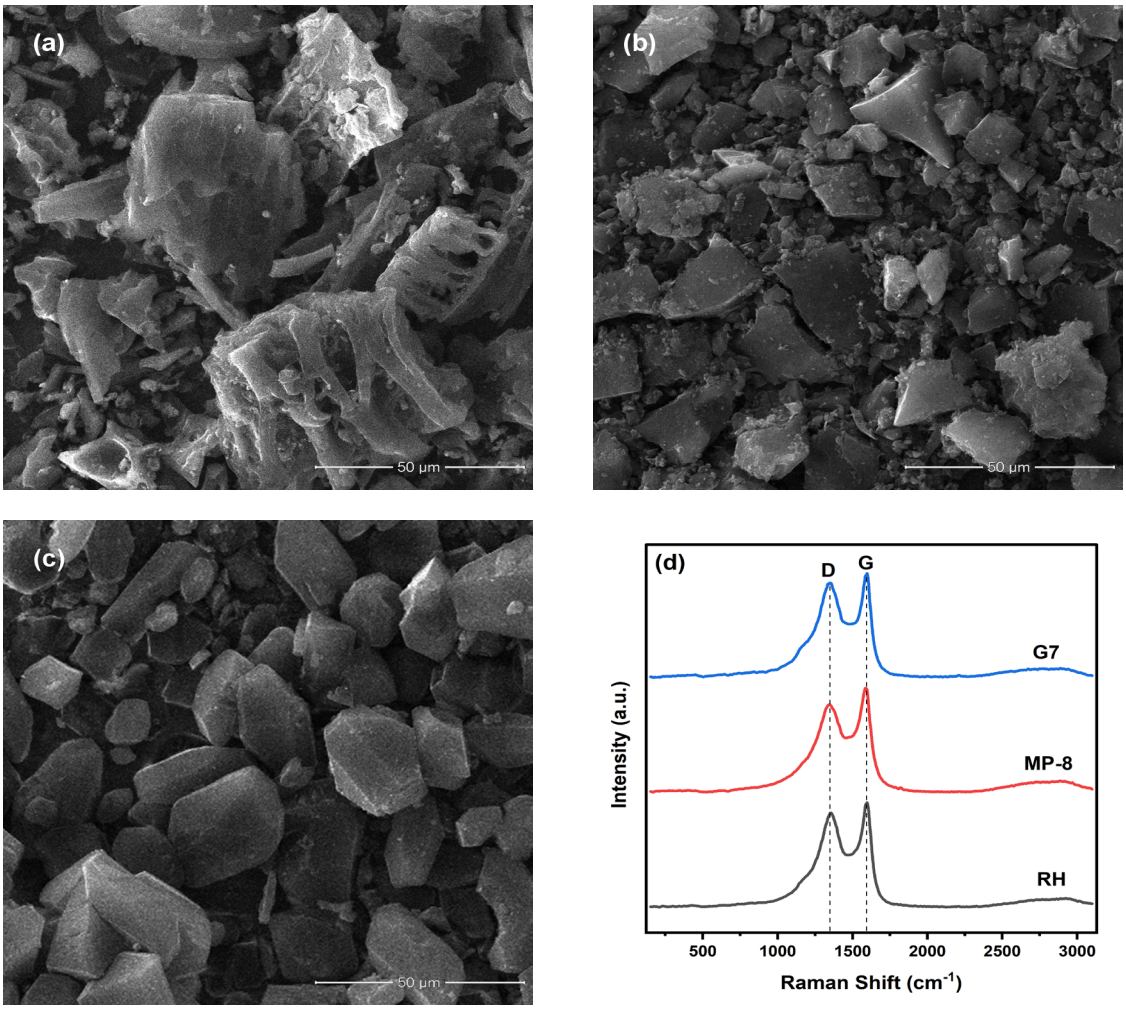

Fig. 1. SEM images of porous carbons: (a) Rice Husk (RH), (b) MP-8, (c) G7, and (d) corresponding Raman spectrum for them.

be seen in Fig. 1(a), activated carbon from rice husk has a developed surface and is characterized by a multitude of large pores, replicating the structure of the organic precursor. The particles of activated carbon have a wide size range from 10 to 50 μm. The average particle size of template carbon derived from magnesium citrate is 12 μm, as shown in Fig. 1(b). Figure 1(c) presents images of template carbon from glucose, whose particles are characterized by distinct boundaries with an average size of 15 μm.

The results of Raman spectroscopy (Fig. 1d) didn't show significant differences. All the obtained samples have similar spectra, confirmed by the results of the Lorentz decomposition presented in Table 2.

Figure 1d shows that all the samples have a high intensity of the D peak, indicating the presence of defects in the carbon structure. This is also evidenced by the intensity ratio of the D and G peaks (ID/IG) [22]. The absence of a distinct 2D peak in the 2600–2800 cm^{-1} range indicates a lack of long-range order in the structure. The appearance of the G band is a characteristic feature of carbon materials with sp^2 bonds. The crystallinity degree and the orderliness of the carbon materials' structure can be assessed by the full width at half maximum (FWHM) of the G band [23].

Table 2. Raman peak decomposition data for the obtained carbon materials

	RH	MP-8	G7
FWHM (D)	229.61	256.08	240.39
FWHM (G)	76.24	83.09	72.01
G,%	26.83	27.24	24.64
ID/IG	0.96	0.93	0.98

In Table 3, the porous characteristics of the obtained carbon materials RH, MP-8, and G7 are presented. The activated carbon derived from rice husk is distinguished by the largest specific surface area (SSA) of 2315 m^2/g and microporosity with an aver-

age pore width <1 nm. Templated carbons MP-8 and G7 have pore sizes around 3.4 and 7.2 nm, respectively. The use of a SiO_2 template with an average nanoparticle size of 7 nm allowed the creation of templated carbon with a controlled pore size and the largest volume of mesopores, approximately 3.5 cm^3/g, as well as a moderately high SSA of 1320 m^2/g. Templated carbon from magnesium citrate has a high SSA of 1976 m^2/g and a large volume of mesopores, which collectively should contribute to greater capacity accumulation.

Table 3. Porosity data of carbon materials RH, MP-8 and G7

Material	S_{BET} (m^2/g)	V_{micro} (cm^3/g)	V_{meso} (cm^3/g)	d (nm)
RH	2315	0.84	0.19	0.9
MP-8	1976	0.40	1.36	1.36
G7	1320	0.52	1.89	1.89

3.2. Three-electrode cell studies

The CV data for each electrode were obtained using a T-type Swagelok three-electrode cell with an Ag/AgCl reference electrode at a scan rate of 2 mV/s and are shown in Fig. 2. To prevent redox reactions on the counter electrode, it mass was five times higher than that of the working electrode. As can be seen from the presented data, in the negative potential region, all electrodes are characterized by charge accumulation only in the electric double layer (EDL). At the same time, reducing the potential to -1.3V leads to a significant increase in current, caused by the process of water decomposition and subsequent hydrogen evolution reaction.

The positive electrode is also characterized by charge accumulation in EDL in the potential range from 0 to 0.6V. However, increasing the potential above these values leads to an increase in current, caused by the Faradaic reactions within the system,

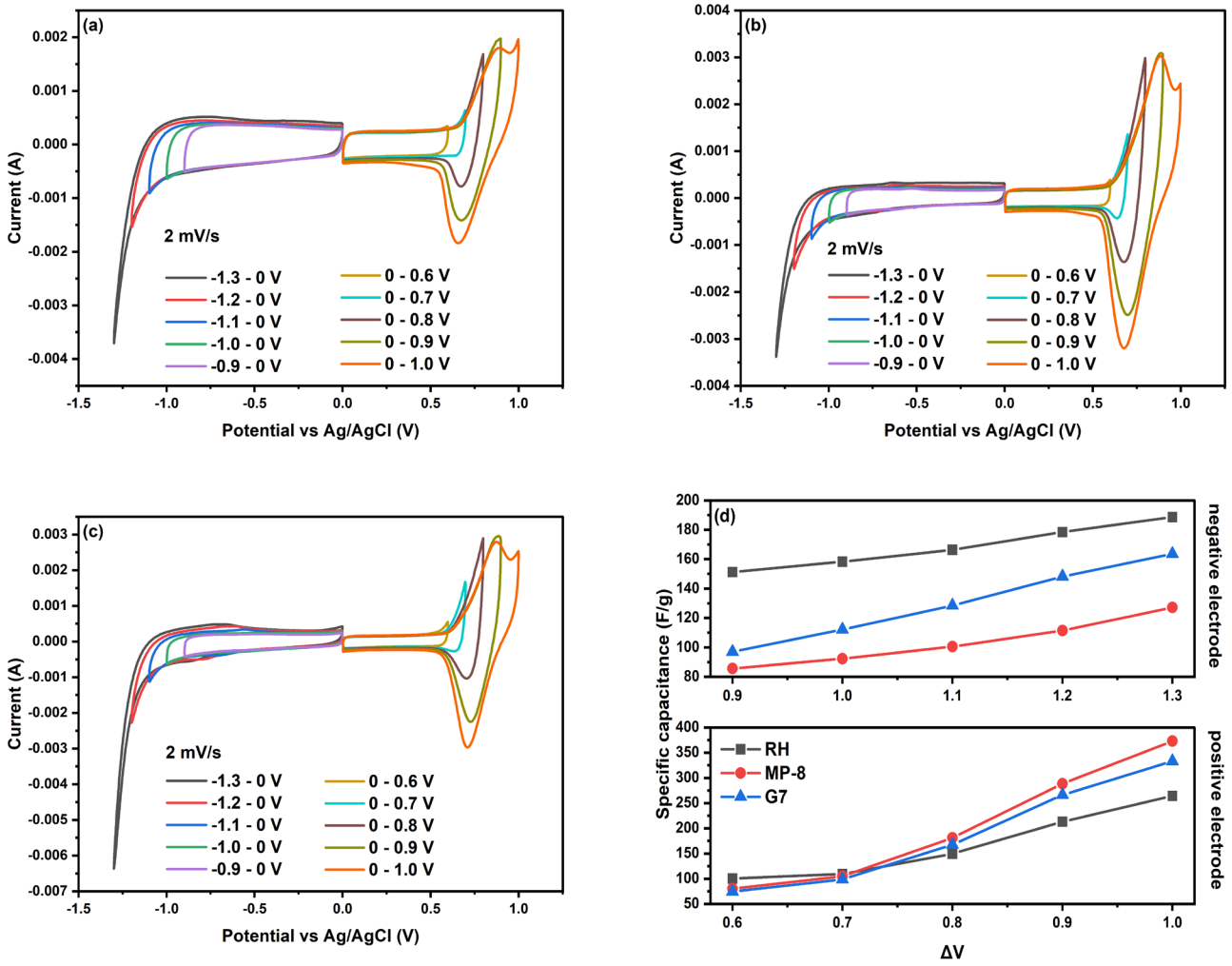

Fig. 2. CV curves for (a) RH, (b) MP-8 and (c) G7 at different potentials and sweep rate of 2 mV/s and (d) dependence of specific capacitance on potential difference (ΔV).

particularly the redox reaction of Br^-/Br_3^- transition. This, in turn, contributes to an increase in the electrode's capacitance (Fig. 2d) [24]. When the potential exceeded 1V, active corrosion of the metallic current collector by bromine was observed, making further voltage increase impossible in this configuration.

To accurately determine the operating voltage limit of the electrodes, the reversibility of the reaction was evaluated by comparing the charge, per CV cycle.

$$\eta = Q_{dis}/Q_{ch} \times 100\% \quad (5)$$

Figure 2d shows the relationship between the specific capacitance and the electrode potential, in the positive and negative potential region.

Based on the data obtained, it is clear that the RH electrode has the highest specific capacitance in the negative potential range, which is 151 F/g with an efficiency of 95% at a voltage of 0.9 V. Template carbons MP-8 and G7 have values of specific capacitance much lower at the same potential. However, they have a significant capacitance advantage in the positive potential region due to larger pore size and volume.

3.2. Full cell studies

Based on the data obtained from three-electrode cells testing, several configurations with balanced electrode masses were assembled. Since the electrode made from RH demonstrated higher specific capacitance values in the negative potential range than the templated carbons, it was chosen as the negative electrode for the hybrid capacitor.

In Fig. 3, CVs of two-electrode cells are presented at various scan rates. As can be seen, all samples exhibit deviations from the ideal rectangular curve shape. Specifically, the system utilizing microporous carbon RH shows a less pronounced redox component compared to other cells. An increase in pore size leads to a significant increase in current due to redox reactions occurring at higher voltage ranges.

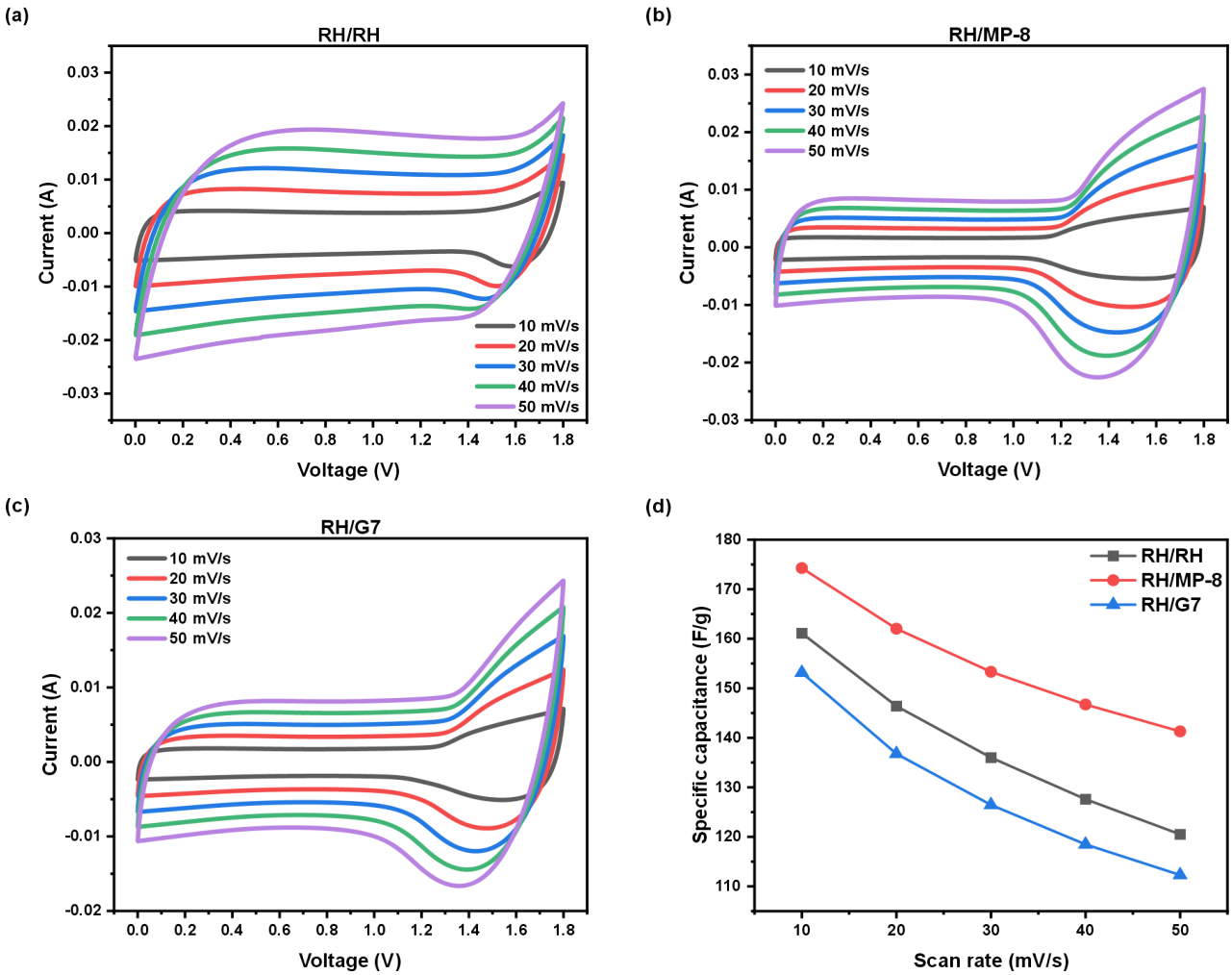

Fig. 3. CV at different scan rates for hybrid capacitors (a) RH-RH, (b) RH-MP-8, (c) RH-G7, and (d) dependence of specific capacitance on scan rates.

As demonstrated in Fig. 3a, at a scan rate of 10 mV/s with the RH sample, a peak attributable to the bromine redox reaction is evident. With increasing scan rates, this peak gradually smoothens, approximating a rectangular shape. This phenomenon can be explained by the diffusion limitations imposed by the micropores (<1 nm) of the activated carbon, which do not allow for the timely adsorption of electrolyte ions. Consequently, electrochemical reactions are confined to the electrode surface, failing to utilize the full internal volume of the pores.

Figure 3(b) and 3(c) show that the redox peak proportionally increases with the scan rate. This may be attributed to the fact that the templated carbons G7 and MP-8 possess a mesoporous structure with pore sizes of 8 nm and 3.5 nm respectively, which are significantly larger than the size of the hydrated ions of the electrolyte. The large pore size facilitates easy adsorption of electrolyte ions into the electrode pores. Consequently, the occurrence of redox reactions is clearly observable in the CV graphs regardless of the scan rate. Comparison of the samples indicates that the RH/RH hybrid capacitor exhibits a substantial double-layer capacitance but considerably less capacitance due to redox reactions (Fig. 3). The increase in scan rate leads to a significant decrease in the specific capacitance of the system (Fig. 3d). We attribute this to the slow kinetics of electrochemical reactions occurring at the electrode surface and transport limitations in charge transfer at high scan rates.

The hybrid capacitor RH/MP-8, which has a positive electrode with significant surface area and pore size, possesses the highest specific capacitance. The RH/RH hybrid capacitor exhibits a lower specific capacitance, presumably due to limitations in electrolyte diffusion. The system comprising the RH/G7 electrode combination also has a lower capacitance, owing to the small surface area of the positive electrode.

Figure 4 (a-c) shows the GCD curves of two-electrode cells at varying current densities. In this case, the redox reactions are facilitated by an electrolyte containing bromine, therefore, the porous structure of carbon plays a significant role in the reaction kinetics. An ideal supercapacitor would exhibit a linear relationship in its galvanostatic charge/discharge curve. However, the occurrence of redox reactions slows down the charge and discharge processes, altering the curve shape at high voltages [10].

As can be observed from Fig. 4 (a-d), the GCD curves of all three hybrid capacitors exhibit a battery-like GCD curve shape. The redox reaction peaks, observed in the CV mode as a current increase, cause a deceleration in the charging rate on the GCD graphs due to the time required for the redox reaction to occur at a fixed current density.

As can be seen in Fig. 4 (e-f), the calculated capacitance values are significantly different from the actual values when only the discharge time is taken into account. The hybrid capacitor with RH/MP-8 electrodes has the highest specific capacitance. When the nonlinearity of the discharge curve is taken into account, the actual capacitance of the RH/G7 capacitor is significantly higher than the direct calculation data, surpassing the RH/RH capacitor in this parameter. The change in specific capacitance of the RH/RH capacitor is not significantly different from the direct time-based calculation because the occurrence of the redox reaction is minimal.

Figure 4 (g-h) shows the specific energy and energy efficiency data. The RH/MP-8 capacitor exhibits the highest energy efficiency compared to the other samples, maintaining an efficiency level of 82% even at current densities above 5 A/g, which is higher than the other systems presented even at lower current densities.

Due to the greater accessibility of the pores in templated carbons for redox reactions, their specific energy values are higher than those of the microporous RH. The specific energy values for the RH/MP-8 capacitor are approximately 27 Wh/kg, while for the RH and G7 systems they are 20 and 23 Wh/kg respectively at 0.5 A/g.

Figure 5 shows the cyclic stability data of the cells at a current density of 2 A/g. This current density maintains high specific performance and has an optimum charge-discharge time for long-term testing.

Figure 5(a) shows a significant increase in Coulomb efficiency during the first 400 cycles, followed by a smooth increase to values above 99% during the cycling process. However, Fig. 5(b) shows a decrease in specific capacitance values by more than 24% for the RH/RH and RH/MP-8 systems as the number of cycles increases. The RH/G7 cell demonstrates the best capacitance retention, maintaining capacitance values at 84% after 5000 cycles. This decrease in capacitance may indicate that during long-term cycling, there is a depletion of the electrolyte due to incomplete reversibility of the redox reaction or shuttle effect, in which the products of the redox reaction irreversibly pass into the electrolyte volume [25].

The performance of the hybrid capacitor with asymmetric electrodes improved compared to the symmetric configuration due to several factors.

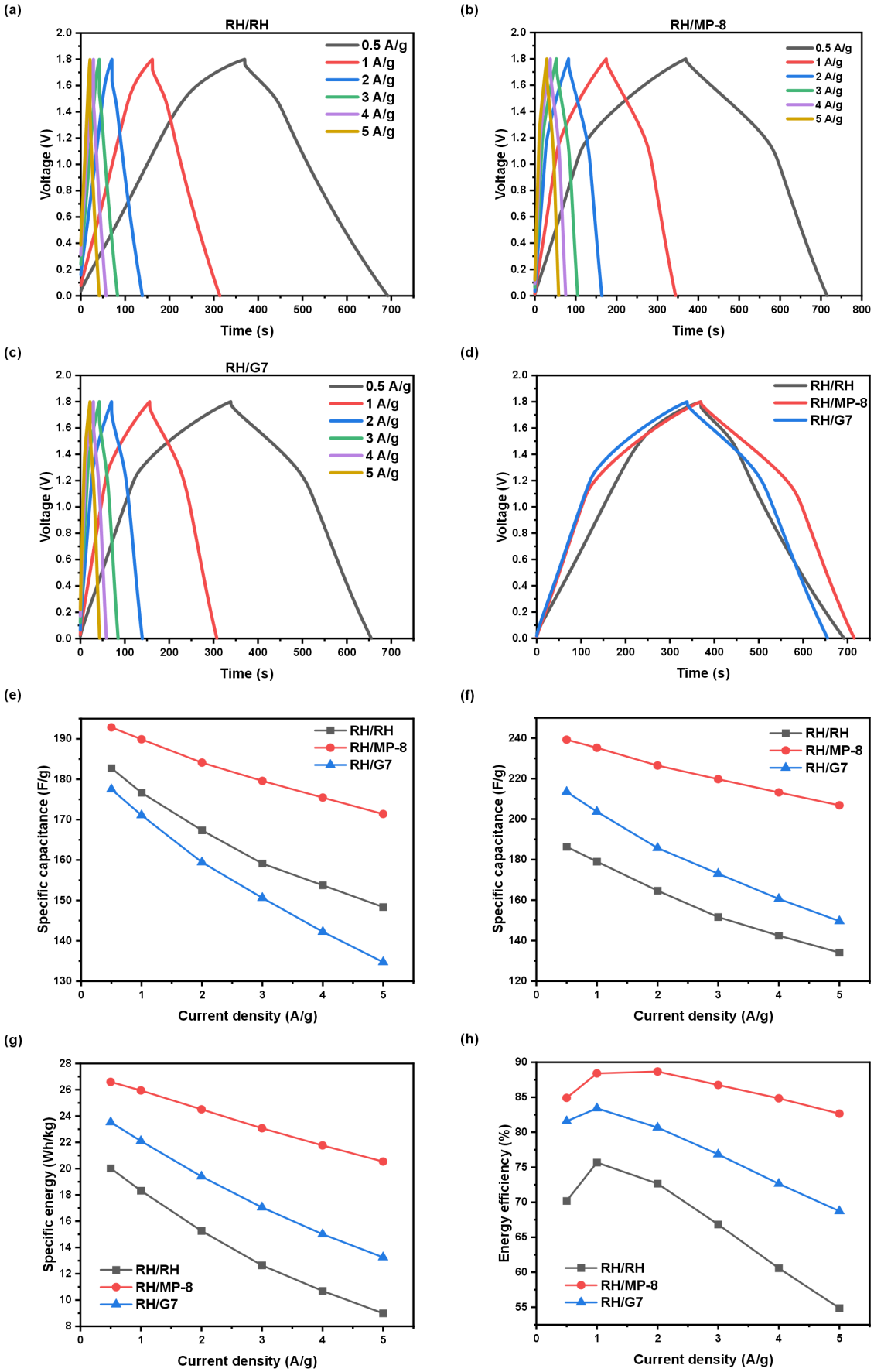

Fig. 4. GCD curves for (a) RH/RH, (b) RH/MP-8, and (c) RH/G7 at various current densities and (d) comparative assessment at 0.5 A/g. Specific capacitance values calculated from GCD curves using (e) the standard equation for EDLC and (f) taking into account the nonlinearity of the discharge curve and (g) dependence of specific energy and (e) energy efficiency on current density.

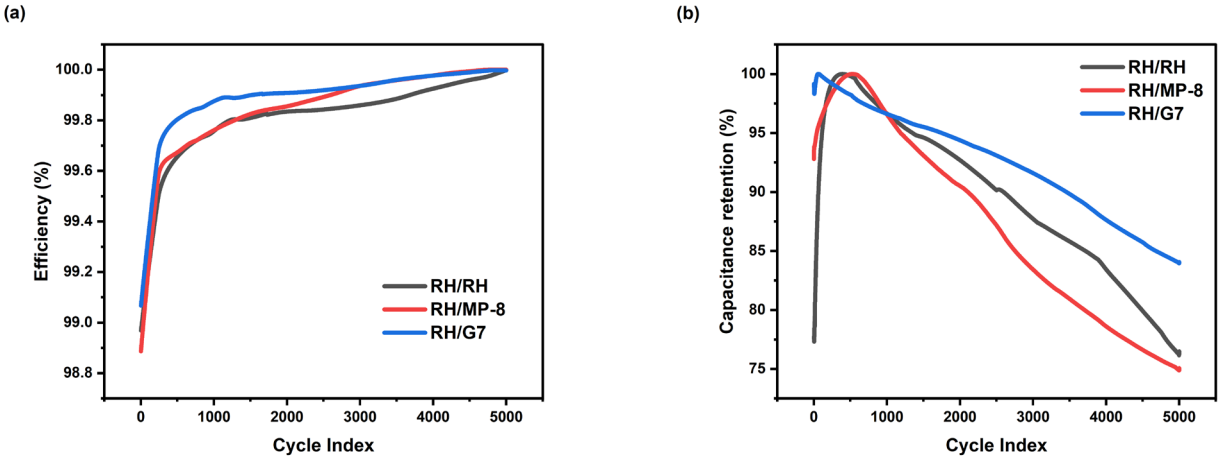

Fig. 5. Cyclic stability of hybrid capacitors at 2 A/g: (a) Coulomb efficiency and (b) capacitance retention.

Firstly, the specific capacitance of the positive electrode changed depending on the porous structure. This was demonstrated in the three-electrode cell, where an increase in capacitance was observed due to the active occurrence of redox reactions in templated carbons with larger pore volumes. Simultaneously, the activated carbon electrode with a microporous structure (RH) may experience limitations in the diffusion of electrolyte ions, which can affect the reaction kinetics. Secondly, the combination of the large surface area of the negative electrode of microporous RH, where the charge is mainly accumulated by the electric double layer (EDL) mechanism, and the positive electrode with a large pore volume allows for an increase in specific capacitance and specific energy by optimizing the electrode mass. This optimization contributes to the overall efficiency of the asymmetric configuration.

Thus, by optimizing the porous structure of the hybrid capacitor and by selecting the most efficient electrode materials of the cathode and anode it was possible to increase the specific capacitance by 54%, the specific energy by 128% and the energy efficiency by 51% at a high current density of 5 A/g comparing to the symmetric RH/RH hybrid capacitor, and the capacitance retention for the Rh/G7 system was improved by 9% for long-term cycling at a current density of 2 A/g.

4. Conclusion

In this study we demonstrated that optimizing the porous electrode structure significantly improves the efficiency of hybrid capacitors. It was shown that microporous carbons suit well as EDLC type electrode, accumulating high capacitance due to their large specific surface area. On the other hand, templated carbons with a mesoporous structure performed well as positive electrodes in the system where the redox reaction occurs, which leads to a significant improvement in energy storage performance. Thus, cells with templated carbon G7, having the lowest surface area as a positive electrode together with RH as a negative electrode, shows better energy storage performance comparing to the symmetric system. The RH/MP-8 hybrid capacitor shows a 54% increase in specific capacitance, 128% increase in specific energy, and 51% increase in energy efficiency at a high current density of 5 A/g comparing to the symmetric RH/RH capacitor, and the capacitance retention for the RH/G7 system was improved by 9% for long-term cycling at a current density of 2 A/g. These data demonstrate the significant role of porous electrode structure in the design of next-generation capacitors. However, it should be noted that large pore sizes are much less able to hold ions in the carbon structure, which increases the chances of shuttling oxidation products into the electrolyte volume, which in the operating conditions can lead to depletion of the electrolyte and to significant decrease of its performance. Therefore, depending on the electrolyte type, a careful selection of the porous electrode structure may be required.

Acknowledgements

V.P. acknowledges the financial support from the Science Committee of the Ministry of Science and Higher Education of the Republic of Kazakhstan (Scientific Research Grant no. AP14872549).

References

[1]. A. Muzaffar, M.B. Ahamed, K. Deshmukh, J. Thirumalai, *Renew. Sust. Energ. Rev.* 101 (2019) 123–145. DOI: 10.1016/j.rser.2018.10.026

[2]. D.P. Chatterjee, A.K. Nandi, *J. Mater. Chem. A* 9 (2021) 15880–15918. DOI: 10.1039/D1TA02505H

[3]. L. Kouchachvili, W. Yaïci, E. Entchev, *J. Power Sources* 374 (2018) 237–248. DOI: 10.1016/j.jpowsour.2017.11.040

[4]. M.B. Camara, H. Gualous, F. Gustin, A. Berthon, *IEEE Trans. Veh. Technol.* 57 (2008) 2721–2735. DOI: 10.1109/TVT.2008.915491

[5]. C. Abbey, G. Joos, *IEEE Trans. Ind. Applicat.* 43 (2007) 769–776. DOI: 10.1109/TIA.2007.895768

[6]. A.G. Olabi, Q. Abbas, A. Al Makky, M.A. Abdelkareem, *Energy* 248 (2022) 123617. DOI: 10.1016/j.energy.2022.123617

[7]. B.E. Conway, Electrochemical Supercapacitors, Springer US, Boston, MA, 1999. DOI: 10.1007/978-1-4757-3058-6

[8]. P. Simon, Y. Gogotsi, *Nat. Mater* 7 (2008) 845–854. DOI: 10.1038/nmat2297

[9]. D.P. Dubal, O. Ayyad, V. Ruiz, P. Gómez-Romero, *Chem. Soc. Rev.* 44 (2015) 1777–1790. DOI: 10.1039/C4CS00266K

[10]. A. Mendhe, H.S. Panda, *Discov. Mater.* 3 (2023) 29. DOI: 10.1007/s43939-023-00065-3

[11]. S. Dong, E.C. La Plante, X. Chen, M. Torabzadegan, et al., *Npj Mater. Degrad.* 2 (2018) 32. DOI: 10.1038/s41529-018-0051-4

[12]. M. Zhong, M. Zhang, X. Li, *Carbon Energy* 4 (2022) 950–985. DOI: 10.1002/cey2.219

[13]. C. Xiong, Y. Zhang, Y. Ni, *J. Power Sources* 560 (2023) 232698. DOI: 10.1016/j.jpowsour.2023.232698

[14]. Z. Zhai, L. Zhang, T. Du, B. Ren, et al., *Mater. Des.* 221 (2022) 111017. DOI: 10.1016/j.matdes.2022.111017

[15]. F. Cheng, X. Yang, S. Zhang, W. Lu, *J. Power Sources* 450 (2020) 227678. DOI: 10.1016/j.jpowsour.2019.227678

[16]. A.P. Silva, A. Argondizo, P.T. Juchen, L.A.M. Ruotolo, *Sep. Purif. Technol.* 271 (2021) 118872. DOI: 10.1016/j.seppur.2021.118872

[17]. V. Pavlenko, S. Kalybekkyzy, D. Knez, Q. Abbas, et al., *Ionics* 28 (2022) 893–901. DOI: 10.1007/s11581-021-04354-w

[18]. Zh. Supiyeva, Kh. Avchukir, V. Pavlenko, M. Yeleuov, et al., *Mater. Today: Proc.* 25 (2020) 33–38. DOI: 10.1016/j.matpr.2019.11.013

[19]. F. Béguin, V. Pavlenko, P. Przygocki, M. Pawlyta, P. Ratajczak, *Carbon* 169 (2020) 501–511. DOI: 10.1016/j.carbon.2020.07.071

[20]. Z. Ayaganov, V. Pavlenko, S.F.B. Haque, A. Tanybayeva, et al., *J. Energy Storage* 78 (2024) 110035. DOI: 10.1016/j.est.2023.110035

[21]. Y. Shao, M.F. El-Kady, J. Sun, Y. Li, et al., *Chem. Rev.* 118 (2018) 9233–9280. DOI: 10.1021/acs.chemrev.8b00252

[22]. R. Guo, C. Lv, W. Xu, J. Sun, et al., *Adv. Energy Mater.* 10 (2020) 1903652. DOI: 10.1002/aenm.201903652

[23]. Y. Yerlanuly, R. Zhumadilov, R. Nemkayeva, B. Uzakbaiuly, et al., *Sci. Rep.* 11 (2021) 19287. DOI: 10.1038/s41598-021-97997-8

[24]. X. Tang, Y.H. Lui, B. Chen, S. Hu, *J. Power Sources* 352 (2017) 118–126. DOI: 10.1016/j.jpowsour.2017.03.094

[25]. W. Yang, Q. Han, W. Li, M. Wu, et al., *Chem. Eng. J.* 448 (2022) 137731. DOI: 10.1016/j.cej.2022.137731